Reliability Assessment of the Switched Reluctance Motor Drive Under Single Switch Chopping Strategy

Hao Chen, *Senior Member, IEEE*, Huan Yang, Yuxiang Chen, and Herbert Ho-Ching Iu, *Senior Member, IEEE*

***Abstract*—In this paper, a detailed set of reliability prediction methodology for switched reluctance motor drive (SRD) considering system specific control strategy and component fault classification is elaborated from component level to system level. At component level, introduction to SRD and its single switch chopping strategy is presented to capture characteristics of SRD reliability under a certain control strategy. The unique fault modes classification and summary methods which are tailored to SRD are applied for identification of system dominant fault modes. Then at system level, binary models (reliability block diagram and part-count model) and multivariate model (Markov model) are adopted to build systematic SRD reliability model, respectively. Especially in the Markov model, state transition diagram and state probability matrix P(t) are built in detailed description to constitute the graphical and numerical Markov reliability model. Conclusions can be drawn that compared with RBD, Markov model can capture the effect of specific control strategy on system reliability, and further demonstrates the stronger consistency with SRD practical operation. Fault simulation and experiments are conducted to illustrate the influence on system operation state caused by a control strategy. Also, the results verify the state assessment of system performance after component-level fault occurs.**

***Index Terms*—Control strategy, fault classification, Markov reliability model, state transition diagram, switched reluctance motor drive (SRD).**

I. Introduction

As a novel electromechanical system, switched reluctance motor drive (SRD) with its excellent fault-tolerant performance has competitive advantages over other drive systems in harsh environments requiring continuous work [1]. Applications include those in aircraft, power generation [2], railway traction [3], hybrid electric vehicles [4], etc. In such safety-critical applications, system failure can cause significant financial losses, environmental degradation, or even life losses [5]; thus, making reliability a grave concern as it directly relates to safety issue. Quantitative reliability prediction of SRD contributes to its application of high reliability. It can find potential safety problems and timely inform of the protection or maintenance measures to avoid catastrophic failure. Also, reliability prediction provides service to comparison of competitive designs, which helps to optimize the design and meet user requirements. However, the special control strategy and operation performance of SRD challenges the reliability prediction model. No techniques have been developed up till now to accomplish this task.

Conceptually, reliability refers to the probability that a system can fulfill its task for intended life under intended operating environments [6], [7]. System reliability is generally quantified by the assessment of reliability indexes. In [8], commonly used reliability indexes are presented, among which reliability function $R(t)$ and mean time to failure (MTTF) rank the top two. To achieve quantitative reliability assessment, reliability prediction models are inevitable [9]. Along with the development of reliability engineering, reliability prediction also has received significant achievements, especially in power electronic systems. Modeling techniques for reliability estimation are divided into two levels, i.e., at component level or at system level [8]. At the component level, empirical-based models and physics-of-failure models are the main two groups [10]–[12]. Comparison between the two types is discussed in depth in [13]. Physics-of-failure models are expert in studying potential failure mechanics to predict end-of-life, but the complexity and high consumption limit their applications in components that belong to a whole system [8], [13]. Empirical-based models may be pessimistic to a certain extent, but show relatively good performance when applied as indicators of field reliability. As for the system level, models commonly used are part-count model, reliability block diagrams (RBDs), fault tree analysis (FTA), and Markov model. A detailed discussion for each of these techniques is found in [14]. In [15], a part-count model is applied to a power converter to study mission profile effect on the reliability. Compared with the part-count model, an FTA is an advisable choice, while analyzing specific failures that have critical importance [16]. RBD is a oneline diagram that illustrates the functional logic relationship between components in a system and commonly used for electric systems [17]. Though simple to operate, these aforementioned modeling techniques are invalid for fault tolerant or repairable systems, as they fail to reflect the impact of control strategy, fault classification, repair process, and order of component failure to reliability [14]. Then, Markov reliability modeling stands out because of its ability to handle this kind of problem.

In Markov reliability modeling, the stochastic process Markov chain is utilized to model systems with several states,

Manuscript received September 1, 2014; revised November 17, 2014; accepted April 29, 2015. Date of publication May 5, 2015; date of current version November 16, 2015. This work was supported in part by the National Natural Science Foundation of China under Grant 51277174, and Special Funds for the Development of Small and Medium-Sized Enterprises on International S&T Cooperation Program between China and Europe under Grant 2014-163-11. Recommended for publication by Associate Editor J. Hur.

H. Chen is with the School of Information and Electrical Engineering, China University of Mining and Technology, Xuzhou 221116, China, and also with the School of Electrical, Electronic and Computer Engineering, The University of Western Australia, Crawley, W.A. 6009, Australia (e-mail: hchen@cumt.edu.cn).

H. Yang and Y. Chen are with the School of Information and Electrical Engineering, China University of Mining and Technology, Xuzhou 221116, China (e-mail: 15152117120@163.com; wxyr1988@163.com).

H. H.-C. Iu is with the School of Electrical, Electronic and Computer Engineering, The University of Western Australia, Crawley, W.A. 6009, Australia (e-mail: herbert@ee.uwa.edu.au).

Digital Object Identifier 10.1109/TPEL.2015.2429557

as well as the transitions between the states [14]. With these properties, a multiple-state Markov chain model has been applied to reliability study of power systems or transmission lines at earlier times [18]–[20]. Initially, the Markov model is established within a relatively small and simple system, such as a single unit or a certain component. Later, with the widely and successful application of a Markov process in power systems, the application has been extended to drive systems; however, most of which are for the induction motor drive system. In [21], a Markov model of a induction motor drive system is developed for reliability calculation, but the system analyzed is shrunk to only three equivalent components. In [22], fault modeling and performance evaluation of an induction motor drive, also the first step to build a Markov reliability model, are elaborated clearly. A complete Markov reliability model for an induction motor drive is developed in [23] to assess reliability index, which provides a comprehensive and versatile reliability modeling technique for motor drive systems. Extended work has incorporated protection system failure into the system reliability evaluation [24], or considered integrating economic aspects in reliability [25], which are beyond the scope of this paper.

Since SRD has been known for its fault operation capability, systematic reliability prediction models that quantify the ability to tolerate faults and assess its overall reliability indexes are essential. However, literatures have not specifically discussed the reliability prediction for SRD. This paper focuses on the task of quantitative reliability prediction for a SRD system. To assess reliability of a certain system, fault mode classification is performed first. In [26], a comprehensive introduction to possible electrical faults in SRD is described, but sensor faults are ignored there. As a supplement, sensor faults are studied in induction motor drives [27], [28] and electric traction power systems [29] provide a reference for SRD fault analysis. As for reliability prediction models, RBD can briefly indicate the logical relationship between functional units and system, which helps calculate system reliability indexes based on each functional units, thus being applied in this paper. Besides, Markov model is also taken in this paper to evaluate SRD reliability, as it has been recognized for its ability of assessing the system performance with multilevel faults and in multilevel operation states, which is in line with the practical operating conditions of SRD.

The remainder of this paper is organized as follows. In Section II, a brief introduction to SRD and its single switch chopping strategy is presented. Also, component-level fault modes identification and failure model establishment are conducted to prepare for the subsequent system reliability modeling. A detailed description of system-level reliability modeling for SRD is presented in Section III. RBD and Markov mode are, respectively, adopted. Specifically, in Markov reliability model, complete system state transition diagram is presented to show a graphical Markov model, and state probability matrix is achieved to represent a numerical Markov model. Results show that the Markov model can capture the effect of specific control strategy on system reliability, and further demonstrates the stronger consistency with SRD practical operation. In Section IV, simulations and experiments are performed to verify the accuracy of the system state evaluation and illustrate the control strategy influence on system operation state. Finally, in Section V, a brief summary of this paper is provided, also directions for future research work are proposed.

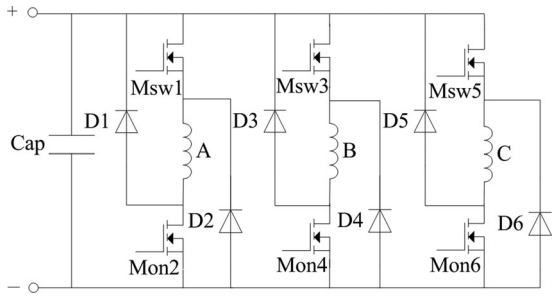

Fig. 1. Three-phase asymmetric bridge converter.

II. Component-Level Dominant Fault Modes for SRD

It is essential to implement component-level fault classification and failure model establishment before the reliability evaluation of a whole system so that the preparation data for system reliability modeling can be achieved. In this section, system composition of SRD is outlined initially, followed by the identification of system key components, which fail frequently and affect system normal operation severely. Then, a comprehensive fault mode analysis is presented. After that component-level failure models are built based on typical reliability models, which provide inputs for system reliability evaluation.

A. Introduction of SRD and Its Control Strategy

A whole SRD system consists of motor, converter, controller, and sensor parts. In this paper, a three-phase switched reluctance motor with 12/8 pole structure is selected to conduct the fault analysis. As for the position sensor, photoelectric sensor which composed of fluted disc and photoelectric switch is selected to provide real-time position information. Photoelectric switches detect relative position of stator and rotor, and then, controller transits this position information into control signal to drive metal–oxide–semiconductor field-effect transistors (MOSFETs) of each phase. Specifically, three photoelectric switches mounted on the stator of the motor, while fluted disc is fixed on the rotor shaft. Make clear that teeth and slots of the fluted disc are exactly consistent with the rotor. Then, the teeth and slots successively pass by the photoelectric switches with the motor's rotating. When the teeth block the photoelectric switch light path, photoelectric switch turns OFF, otherwise, it turns ON. These on or off signals are processed by logic circuit, thus producing real-time rotor position information. The position signal provides pivotal information for the controller to directly trigger MOSFETs in a certain phase, thus completing position closed-loop control.

Besides, the widely used three-phase asymmetric bridge converter is applied, which is shown in Fig. 1. Meanings of the

letter symbols in Fig. 1 are illustrated as follows: *Cap* is the dc bus capacitor; *D1–D6* are six freewheeling diodes; the letters *A–C,* respectively, represent windings of each phase; symbols with the first letter *M* signify power transistors, here the transistors are selected to be MOSFET. In a certain phase, Msw and Mon, respectively, indicate upper and lower MOSFET, and this definition is determined by the control strategy.

Here, in order to reduce torque ripple and power losses, single switch chopping strategy is adopted. Taking *Phase A* as an example, Msw1 is driven by the pulse width modulation (PWM) chopping signal, and the drive signal of Mon2 is the position control signal. During on period of each phase, Mon2 remains ON, while Msw1 implements chopping; and in the freewheeling period, both transistors are turned OFF [30]. It is noted that the upper and lower MOSFETs are treated as two different kinds of components in the system, because the single switch chopping control strategy divides their functions into two different categories. Also, their faults would cause different effects on system operation states as well as system reliability, which verify the dependence of the system reliability on control strategy.

In addition, the fault-tolerance ability of SRD indicates that the controller itself is capable of fault detection and isolation. Generally, in SRD fault diagnosis, additional sensors are used to get more fault features such as fault current information [31], but potential faults of the additional sensors may put extra burden to system reliability. Hence, from the point of system reliability, software algorithm diagnosis method is recommended [32], which is the exact case adopted in this paper. Together with the diagnosis technique, fault tolerant control is then applied to ensure the continued operation after certain faults [33]–[35].

B. Dominant Fault Modes Classification and Summary

In this section, a specific fault classification and summary approach is applied for identification of SRD dominant fault modes in key components. The key components in a system are those that withstand higher thermal and electrical stress; thus, being more easily to fail, also their failures are more destructive that may cause the system operation to unexpected pause or stop. As for SRD, power converter, stator windings, current sensor, and position sensor compose system key parts [26]. Among these components, the former two belong to power section, and the latter two are sensor part.

Fault modes classification is implemented to identify the system dominant fault modes in key components. As for power components, open circuit and short circuit are primarily considered, such as in stator windings, dc bus capacitor, power transistor, as well as diode [36]–[38]. Sensor faults include signal omission, signal gain, and constant output [23]. The main fault modes in SRD and their acronym symbols are defined in Table I.

Sometimes several fault modes cause system into the same operation condition. In SRD, five kinds of fault modes will result in system phase-deficient (PD) operation, which includes open circuit in Mon (MonO) and Msw (MswO), short circuit in freewheeling diode (DS), short circuit in windings (WS), and open circuit in windings (WO) [26]. Hence, opposed to fault modes classification, fault modes summary is to collect those fault modes into one and consider them as a whole. Therefore, these five fault modes are merged into PD, as detailed in Table I.

TABLE I
KEY COMPONENTS FAULT MODES OF SRD

Classification	Components	Fault modes and symbols
Power section	Capacitor	Open circuit (CO)
		Short circuit (CS)
	MOSTET Mon	Short circuit (MonS)
	MOSTET Msw	Short circuit (MswS)
	Freewheeling diode	Open circuit (DO)
Sensor part	Current sensor	Omission (CSO)
		Constant (CSC)
		Gain(CSG)
	Position sensor	Omission (PSO)
		Constant (PSC)
		Gain (PSG)
Special case in SRD	PD fault	MonO, MswO, DS, WO, WS (PD)

C. Component-Level Failure Models

Among component-level failure models, the main two groups are physics-of-failure models and empirical-based models. Empirical-based models are built on the foundation of historical data and the constant failure rate, and show relatively good performance when applied as indicators of field reliability [39], [40]. Therefore, the empirical-based models are applied in this paper to build the SRD system reliability model.

Empirical-based models generally take the following (1) to calculate component failure rate, which is the product of component base failure rate λ_b and its relative environment stress factor

$$\lambda_p = \lambda_b \pi_E \pi_Q \prod_i \pi_i \tag{1}$$

where λ_p is the component failure rate during field work; π_E and π_Q are the correction factors, which reflect the influence of external environment and component internal quality; π_i sums up the impact of other factors adjusted with the actual application, such as work environment temperature, internal construction, voltage stress in a power switch, capacitance factor in a capacitor, etc. More detailed information can be found in [39]–[41].

According to (1) and actual operational environment, failure rates of key components on SRD are achieved and listed in Table II. It is worth mentioning that the aim of this paper is to seek a more suitable and general method for SRD reliability prediction; then, the sense of the failure rates is to illustrate the prediction methods rather than their specific values. Therefore, the relative values counts more than the specific absolute values. In this case, it is easier to replace constant failure rates with nonconstant failure ones according to external environments, which provides direction for future work.

TABLE II
FAILURE RATE OF COMPONENT FAULT MODE

Failure rate	Values/hour	Failure rate	Values/hour
λ_{CO}	4.3486×10^{-8}	λ_{DO}	1.14×10^{-9}
λ_{CS}	2.12314×10^{-7}	λ_{DS}	9.3312×10^{-10}
λ_{MonS}	5.493×10^{-7}	$\lambda_{CSZ}, \lambda_{CSC}, \lambda_{CSG}$	4.2×10^{-8}
λ_{MonO}	6.278×10^{-7}	$\lambda_{PSZ}, \lambda_{PSC}, \lambda_{PSG}$	8.18×10^{-8}
λ_{MswS}	7.327×10^{-7}	$\lambda_{WO}, \lambda_{WS}$	1.082×10^{-7}
λ_{MswO}	8.373×10^{-7}		

Fig. 2. RBD model for SRD.

III. SYSTEM-LEVEL RELIABILITY MODELS

Commonly used system reliability models contain binary models and multivariate ones. Binary models assume that the system is in either functioning state or failed one. Part-count models, RBD, and FTA are classified into the binary models. As for the multivariate models, the dynamic stochastic process is introduced, and the system operation process is considered as a state transition process, such as Markov reliability models. It is believed that the system can be in multiple states and can also transit between these multiple states. These two types of models are both applied in this paper to evaluate the SRD reliability.

A. Binary Reliability Models

RBD is a composed of blocks and connection lines, where blocks represent the key components and lines are for logic relationship. The whole model indicates logic relationship of function between components and system. The RBD model for SRD is a series one and contains six component units: stator windings, dc bus capacitor, power switches, freewheeling diode, current sensor, and position sensor, as shown in Fig. 2.

For the series structure SRD system, reliability indexes can be calculated by a part-count method. In part-count models, the constant failure rate that follows the exponential distribution would be adopted [42].

Then, the reliability function *R*(*t*) is

$$R(t) = \prod_{i=1}^{n} e^{-\lambda_i t} = e^{-\sum_{i}^{n} \lambda_i \cdot t} \tag{2}$$

where *n* is the total components number of the system; λ_i is the component failure rate of the *i*th component; and *t* represents time in hours.

According to [39] and the failure rates listed in Table II, the *i*th component failure rate can be achieved by adding the rates of all its fault modes. For example, λ_{CO} and λ_{CS}, respectively, indicate the failure rate of capacitor open-circuit fault and short-circuit fault, then addition of the two will get the capacitor failure rate. The same calculation method is applicable to get the other four components failure rates, except for power switches, where open-circuit fault and short-circuit fault make up 75% of the total fault modes [39]. With these *i*th component failure rates, then according to (2), the reliability function $R_D(t)$ of SRD calculated from RBD is

$$R_D(t) = \prod_{i=1}^{6} e^{-\lambda_i t} = e^{-4.5085t} \tag{3}$$

where subscript *D* in $R_D(t)$ indicates the reliability function calculated by RBD, λ_i is the SRD component failure rate, *e* is the base of exponential function, and *t* represents time in 10^6 h.

B. Multivariate Reliability Model

With excellent fault tolerance, SRD can continue operation despite faults occurred in motor windings or inverter circuitry. Therefore, a single-component fault is not equivalent to system failure, which is beyond the problem solving scope of binary model. It is essential to introduce a multivariate model into reliability prediction for SRD.

Markov reliability model is qualified by individually evaluating the system performance after each component fault and determining system states. First, the system key components and their main fault modes are outlined, which has been conducted in Section II. Second, acceptable parameter boundaries are set as a performance criterion to evaluate the state of the system operation. Then, system states can be assessed. Specifically, a component fault mode is injected into the healthy system before fault analysis is performed, followed by the comparison of the system performance parameters with the parameter boundaries to judge the system state to be "survival" or "failed." If the system survives, a second-level fault is injected to continue the judgement of system states, and the fault injection is conducted until the system becomes completely ineffective.

1) System State Assessment Under Component Fault: Since SRD may continue running even if a certain component fails, then postfault operation state treatment is a question for SRD reliability assessment. In Markov reliability model, postfault operation state is considered as a system survival state. To evaluate the system state, an overall system fault model is built by injecting component fault models into the healthy system to replace the original ones [26], [27]. Then, a unified performance metrics is set for evaluation of the system postfault operation.

In this paper, a three-phase 12/8 SRD prototype and an asymmetrical half-bridge power converter are selected to assess system states. To achieve a speed closed-loop control, an incremental fuzzy controller and a single switch chopping strategy are adopted to regulate the PWM duty cycle of voltage. The PWM carrier frequency is set to be 3 kHz. Other rated parameters of the SRD prototype are as follows: the rated voltage is 12 V and the rated power is 100 W. In the simulation, the stator windings resistor is set to be 0.45 Ω, and the motor turn-on angle $\theta_{on} = -2°$, turn-off angle $\theta_{off} = 20°$.

TABLE III
PERFORMANCE METRICS

Performance parameter	Acceptable boundary
Speed	Command speed ± 20 r/min
Phase Current	Command current peak ± 4 A

TABLE IV
SYSTEM STATE ASSESSMENT AFTER THE FIRST-LEVEL FAULT

System state	Symbol representation	Fault modes occurred in the system
Survival states	S	CO, PD, MonS, CSC, CSG
Failed states	F	CS, MswS, DO, CSZ, PSZ, PSC, PSG

Basically, the performance metrics are not permanent, and they vary with different actual operating conditions or user requirements. In this paper, the incremental fuzzy controller is adopted to regulate the speed fluctuation in an acceptable range, then this acceptable speed range is set to be parameter metrics. Besides, the current metrics are set in consideration of the system safety. Since the experiments in Section IV may produce high transient impulse current and does damage to the system, then current metrics are set rather conservatively. In summary, considering the control strategy and system safety margin, performance metrics for the selected SRD are listed in Table III. Note that the flexibility of setting metrics exactly leads to the limitation of specific values.

Running the system fault model with a certain fault mode and detecting performance parameters can help to evaluate the system state. After the component fault occurs, system parameters are detected and compared with the performance metrics. If the fluctuation of detected parameters is within the boundary, system is allowed a continued operation and system survives; otherwise, system fails and enters "failed state." For the "survival state," a second-level fault will be injected into the system until system fails completely [23].

Through simulations and experiments, which will be elaborated in Section IV, system states after first-level fault are listed in Table IV. There are 12 kinds of fault modes analyzed. Among these fault modes, seven kinds of faults cause system fail to operate and falls into "failed states," denoted by F; five kinds of fault modes just slightly affect the system performance and would not interrupt the system operation; thus, system enters "survival state," denoted by S. As for the five survival states, a second-level fault is injected to continue the state assessment. It is pointed out that a second-level fault in the same component is not application [23]. Comparison of the system performance with the set performance metrics shows that system completely fails under any third-level fault.

It has been mentioned before that due to the single switch chopping strategy, Mon and Msw are considered as two components. As a result, short circuit occurred in the two components has produced different effects. System that is in survival state under a MonS short-circuit fault, and MswS short-circuit fault causes system to enter into failed state.

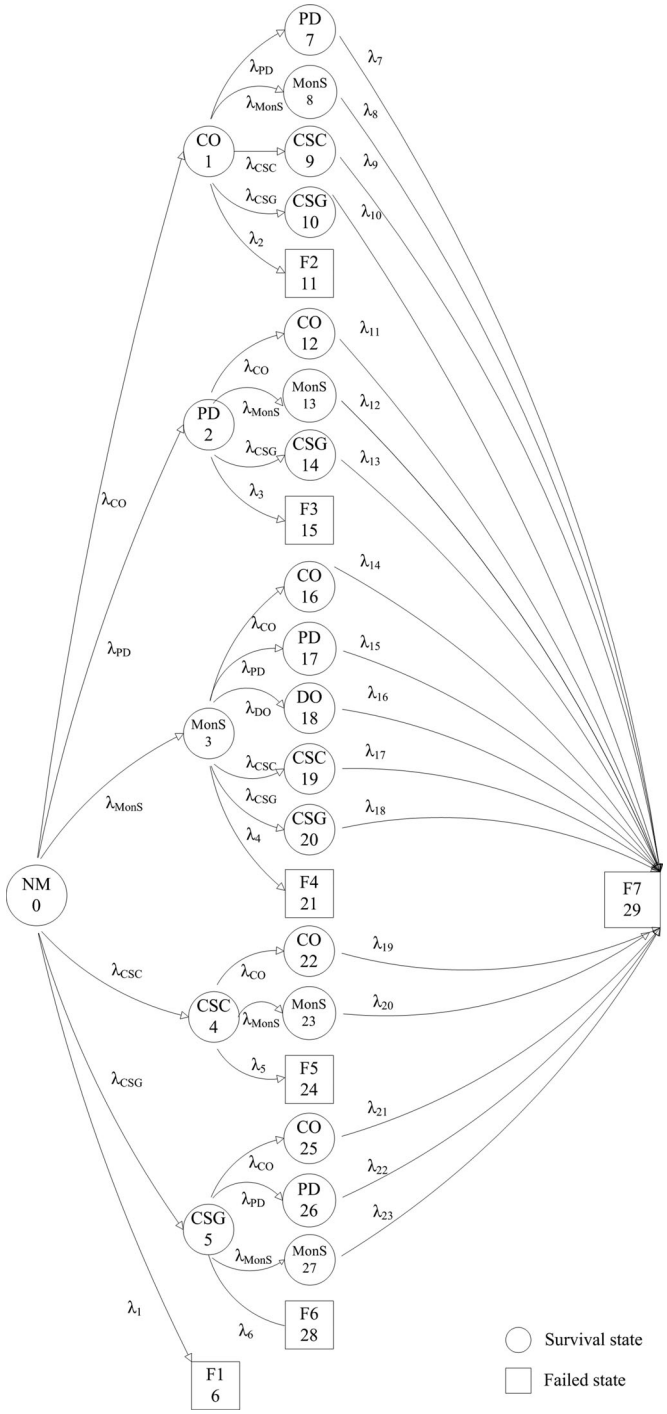

Fig. 3. State transition diagram for SRD.

2) System State Transition Diagram: The collection of all system states is named *state space* and is denoted by a certain set S. For a system comprising $(m+1)$ states, the value of S is arabic numbers, namely $S = \{0, 1, 2, \ldots, m\}$ [21]. According to the above system states assessment of SRD, a state transition diagram is established and shown in Fig. 3, which is the

TABLE V
MEANINGS OF F1–F7 IN STATE TRANSITION DIAGRAM

Symbol	Failure modes included in the symbol
F1–6	State 6, seven fault modes included:CS, MswS, DO, CSZ, PSZ, PSC, PSG
F2–11	State 11, six fault modes included, MswS, DO, CSZ, PSZ, PSC, PSG
F3–15	State15, eight fault modes included:CS, MswS, DO, CSZ, CSC, PSZ, PSC, PSG
F4–21	State 21, six fault modes included:CS, MswS, CSZ, PSZ, PSC, PSG
F5–24	State 24, seven fault modes included:CS, PD, MswS, DO, PSZ, PSC, PSG
F6–28	State 28, six fault modes included:CS, MswS, DO, PSZ, PSC, PSG
F7–29	State 29, a total failed state after third level fault occurs

graphical Markov model. It is composed by all system states together with the transition rates between them, and shows the system state transition process after a component fault occurs.

It can be shown in Fig. 3, initially system state is the normal operation one, denoted by NM-*0*. Here, the symbol *NM* tells system current state and the number *0* is the sequence number. When different first-level faults occur, system falls into different states: five survival states including CO-1, PD-2, MonS-3, CSC-4, CSG-5, and one failed state F1–6 that lumps seven kinds of independent failed states. As for the above five survival states, a second-level fault occurs, and then the system produces 22 kinds of states: 17 survival states and five failed states, which include F2–11, F3–15, F4–21, F5–24, and F6–28. For the 17 survival states, once the system suffers a third-level fault, it gets completely ineffective and the system states converge to one kind of failed state labeled as F7–29.

In Fig. 3, the nodes represent the states (failed or survival), and the arrows represent state transitions triggered by component faults. As for the nodes, the round frame represents survival state, while rectangular frame is for failed state. Symbol inside the frame indicates current state, with the sequence number inside to help label different states. The symbol of alphanumeric combination conveys information of two types of system states: survival or failed. For survival states represented by round frames, except the initial state NM-0, the inside symbols individually indicate a certain fault mode, which causes system to transit into the current state. Correspondence of survival state symbols and fault modes is consistent with Table I. As for failed states, symbols from F1–6 to F7–29 represent a summary of several failed states, i.e., a system transits to the same failed state after several different fault modes, the specific correspondence between the symbols and their containing states are listed in Table V.

Also, in Fig. 3, the arrows connected between two different states indicate the direction of state transition. λ is the state transition rate and equals to the failure rate of the component which occurs fault [14]. Subscript of λ illustrates the meaning of that failure rate, subscript of letter is the fault mode, such as λ_{CO} means failure rate of capacitor open faults; numerical subscripts λ_1–λ_{23} represent a summary of several failure rates. Taking λ_1 as an example, it can be seen from the above Table V that state F1–6 lumps seven fault modes: CS, MswS, DO, CSZ, PSZ, PSC, and PSG, so λ_1 equals to the summary of all these seven failure rates. The specific summary relationship for each failed state is listed in Table VI.

TABLE VI
SUMMARY RELATIONSHIP OF λ_1–λ_{23} IN THE STATE TRANSITION DIAGRAM

Failure rate	Summary relationship
λ_1	$\lambda_{\mathrm{CS}}+\lambda_{\mathrm{MswS}}+\lambda_{\mathrm{DO}}+\lambda_{\mathrm{CSZ}}+\lambda_{\mathrm{PSZ}}+\lambda_{\mathrm{PSC}}+\lambda_{\mathrm{PSG}}$
λ_2	$\lambda_{\mathrm{MswS}}+\lambda_{\mathrm{DO}}+\lambda_{\mathrm{CSZ}}+\lambda_{\mathrm{PSZ}}+\lambda_{\mathrm{PSC}}+\lambda_{\mathrm{PSG}}$
λ_3	$\lambda_{\mathrm{CS}}+\lambda_{\mathrm{MswS}}+\lambda_{\mathrm{DO}}+\lambda_{\mathrm{CSZ}}+\lambda_{\mathrm{CSC}}+\lambda_{\mathrm{PSZ}}+\lambda_{\mathrm{PSC}}+\lambda_{\mathrm{PSG}}+\lambda_{\mathrm{DO}}$
λ_4	$\lambda_{\mathrm{CS}}+\lambda_{\mathrm{MswS}}+\lambda_{\mathrm{CSZ}}+\lambda_{\mathrm{PSZ}}+\lambda_{\mathrm{PSC}}+\lambda_{\mathrm{PSG}}$
λ_5	$\lambda_{\mathrm{CS}}+\lambda_{\mathrm{PD}}+\lambda_{\mathrm{MswS}}+\lambda_{\mathrm{DO}}+\lambda_{\mathrm{PSZ}}+\lambda_{\mathrm{PSC}}+\lambda_{\mathrm{PSG}}$
λ_6	$\lambda_{\mathrm{CS}}+\lambda_{\mathrm{MswS}}+\lambda_{\mathrm{DO}}+\lambda_{\mathrm{PSZ}}+\lambda_{\mathrm{PSC}}+\lambda_{\mathrm{PSG}}$
λ_{17}, λ_{11}	$\lambda_{\mathrm{MonS}}+\lambda_{\mathrm{MswS}}+\lambda_{\mathrm{DO}}+\lambda_{\mathrm{CSZ}}+\lambda_{\mathrm{CSC}}+\lambda_{\mathrm{CSG}}+\lambda_{\mathrm{PSZ}}+\lambda_{\mathrm{PSC}}+\lambda_{\mathrm{PSG}}$
λ_8, λ_{14}	$\lambda_{\mathrm{PD}}+\lambda_{\mathrm{DO}}+\lambda_{\mathrm{CSZ}}+\lambda_{\mathrm{CSC}}+\lambda_{\mathrm{CSG}}+\lambda_{\mathrm{PSZ}}+\lambda_{\mathrm{PSC}}+\lambda_{\mathrm{PSG}}$
λ_9, λ_{10}, λ_{19}, λ_{21}	$\lambda_{\mathrm{PD}}+\lambda_{\mathrm{MonS}}+\lambda_{\mathrm{MswS}}+\lambda_{\mathrm{DO}}+\lambda_{\mathrm{PSZ}}+\lambda_{\mathrm{PSC}}+\lambda_{\mathrm{PSG}}$
λ_{12}, λ_{15}	$\lambda_{\mathrm{CO}}+\lambda_{\mathrm{CS}}+\lambda_{\mathrm{DO}}+\lambda_{\mathrm{CSZ}}+\lambda_{\mathrm{CSC}}+\lambda_{\mathrm{CSG}}+\lambda_{\mathrm{PSZ}}+\lambda_{\mathrm{PSC}}+\lambda_{\mathrm{PSG}}$
λ_{13}, λ_{22}	$\lambda_{\mathrm{CO}}+\lambda_{\mathrm{CS}}+\lambda_{\mathrm{DO}}+\lambda_{\mathrm{MonS}}+\lambda_{\mathrm{MswS}}+\lambda_{\mathrm{PSZ}}+\lambda_{\mathrm{PSC}}+\lambda_{\mathrm{PSG}}$
λ_{16}	$\lambda_{\mathrm{CO}}+\lambda_{\mathrm{CS}}+\lambda_{\mathrm{PD}}+\lambda_{\mathrm{CSZ}}+\lambda_{\mathrm{CSC}}+\lambda_{\mathrm{CSG}}+\lambda_{\mathrm{PSZ}}+\lambda_{\mathrm{PSC}}+\lambda_{\mathrm{PSG}}$
λ_{17}, λ_{18}, λ_{20}, λ_{23}	$\lambda_{\mathrm{CO}}+\lambda_{\mathrm{CS}}+\lambda_{\mathrm{PD}}+\lambda_{\mathrm{DO}}+\lambda_{\mathrm{PSZ}}+\lambda_{\mathrm{PSC}}+\lambda_{\mathrm{PSG}}$

3) State Transition Rate Matrix $\mathbf{\Phi}$*:* The system state transition diagram provides the transition rates between system states. Based on the rates and their connected states, Φ can be established, which contributes to calculate the state probability matrix $\mathbf{P}(t)$. In a $(m+1)$ states system, the system state space is $S=\{0, 1, 2, \ldots, m\}$. For $i, j \in S$, $\varphi_{i(j)}$ is defined as system transition rate from state i to state j, which indicates the component failure rate. Arrange the transition rate $\varphi_{i(j)}$ as a matrix

$$\mathbf{\Phi}_{(m+1)\times(m+1)}=\begin{pmatrix}\phi_{0(0)} & \phi_{0(1)} & \cdots & \phi_{0(m)}\\ \phi_{1(0)} & \phi_{1(1)} & \cdots & \phi_{1(m)}\\ \vdots & \vdots & \vdots & \vdots\\ \phi_{m(0)} & \phi_{m(1)} & \cdots & \phi_{m(m)}\end{pmatrix} \tag{4}$$

and for these diagonal elements $\varphi_{i(i)}$

$$\phi_{i(i)}=-\sum_{\substack{i=0\\ j\neq i}}^{m}\phi_{i(j)} \tag{5}$$

where $-\varphi_{i(i)}$ is the total departure rate from state i. It is noted that the sum of entries in row i is equal to zero [14].

In Fig. 3, the system has a total of 30 states, which in theory generates a transition rate matrix $\mathbf{\Phi}_{30\times30}$. However, the seven failed states F1–6, F2–11, F3–15, F4–21, F5–24, F6–28 and F7–29 do not transit into any states, so the entries of these seven rows are zero. Also, further analysis shows that system reliability is only associated with the survival states, regardless of the failed ones. Therefore, it is essential to eliminate these failed states from $\mathbf{\Phi}_{30\times30}$ in rows and columns. As there are

TABLE VII
NONZERO ELEMENTS OF SIMPLIFIED STATE TRANSITION RATE MATRIX $\mathbf{\Phi}^*_{23\times23}$

Elements	Values
$\varphi_{0(0)}$	$-(\lambda_{CO}+\lambda_{PD}+\lambda_{MonS}+\lambda_{CSC}+\lambda_{CSG}+\lambda_1)$
$\varphi_{0(1)}$, $\varphi_{2(10)}$, $\varphi_{3(13)}$, $\varphi_{4(18)}$, $\varphi_{5(20)}$	λ_{CO}
$\varphi_{0(2)}$, $\varphi_{1(6)}$, $\varphi_{3(14)}$, $\varphi_{5(21)}$	λ_{DP}
$\varphi_{0(3)}$, $\varphi_{1(7)}$, $\varphi_{2(11)}$, $\varphi_{4(19)}$, $\varphi_{5(22)}$	λ_{MonS}
$\varphi_{0(4)}$, $\varphi_{1(8)}$, $\varphi_{3(16)}$	λ_{CSC}
$\varphi_{0(5)}$, $\varphi_{1(6)}$, $\varphi_{1(9)}$, $\varphi_{2(12)}$, $\varphi_{3(17)}$	λ_{CSG}
$\varphi_{3(15)}$	λ_{DO}
$\varphi_{1(1)}$	$-(\lambda_{PD}+\lambda_{MonS}+\lambda_{CSC}+\lambda_{CSG}+\lambda_2)$
$\varphi_{2(2)}$	$-(\lambda_{CO}+\lambda_{MonS}+\lambda_{CSC}+\lambda_3)$
$\varphi_{3(3)}$	$-(\lambda_{CO}+\lambda_{PD}+\lambda_{DO}+\lambda_{CSC}+\lambda_{CSG}+\lambda_4)$
$\varphi_{4(4)}$	$-(\lambda_{CO}+\lambda_{MonS}+\lambda_5)$
$\varphi_{5(5)}$	$-(\lambda_{CO}+\lambda_{PD}+\lambda_{MonS}+\lambda_6)$
$\varphi_{6(6)}$, $\varphi_{10(10)}$	$-\lambda_7$
$\varphi_{7(7)}$	$-\lambda_8$
$\varphi_{8(8)}$, $\varphi_{9(9)}$, $\varphi_{18(18)}$, $\varphi_{20(20)}$	$-\lambda_9$
$\varphi_{11(11)}$, $\varphi_{14(14)}$	$-\lambda_{12}$
$\varphi_{12(12)}$, $\varphi_{21(21)}$	$-\lambda_{13}$
$\varphi_{15(15)}$	$-\lambda_{16}$
$\varphi_{16(16)}$, $\varphi_{17(17)}$, $\varphi_{19(19)}$, $\varphi_{22(22)}$	$-\lambda_{17}$

seven failed states altogether, thus the simplified matrix $\mathbf{\Phi}^*_{23\times23}$ is obtained after the elimination. Note that the elements in the new matrix $\mathbf{\Phi}^*_{23\times23}$ has been renumbered in order. For example, F1–6 is a failed state so the sixth rows and columns of $\mathbf{\Phi}_{30\times30}$ are eliminated, then the original entries $\varphi_{7(7)}$ in $\mathbf{\Phi}_{30\times30}$ are renumbered as $\varphi_{6(6)}$ in $\mathbf{\Phi}^*_{23\times23}$, other elements are also renumbered in this way. Furthermore, in the state transition diagram, the transitions only exist between minority connected states, which means $\mathbf{\Phi}^*_{23\times23}$ is a sparse matrix. The nonzero elements in matrix $\mathbf{\Phi}^*_{23\times23}$ are shown in Table VII.

4) System State Probability Matrix P(t): Followed by $\mathbf{\Phi}^*_{23\times23}$, the state probability matrix $\mathbf{P}(t)$ can be obtained, which forms the numerical Markov model. It provides probability of system in a given state i at any given time t. For a system comprising $(m+1)$ states, the elements of $\mathbf{P}(t)$ are

$$P(t)_{1\times(m+1)} = \begin{bmatrix} P_0(t) & P_1(t) & \cdots & P_m(t) \end{bmatrix} \tag{6}$$

where the element $P_i(t)$ is the probability of system in state i at time t, wherein $i\in(m+1)$.

$\mathbf{P}(t)$ can be solved by the *Chapman–Kolmogorov* equations [14], [23]. In order to eliminate unnecessary calculations in reliability metrics computation, $\mathbf{\Phi}^*_{23\times23}$ is utilized to obtain survival state probability matrix $\mathbf{P}^*(t)$:

$$\mathbf{P}^{*\mathrm{T}}(t) = e^{\mathbf{\Phi}^{*\mathrm{T}}t}\cdot\mathbf{P}^{*\mathrm{T}}(0) \tag{7}$$

where $\mathbf{P}^{*\mathrm{T}}(t)$ and $\mathbf{\Phi}^{*T}(t)$, respectively, are transposed matrix of $\mathbf{P}^*(t)$ and $\mathbf{\Phi}^*(t)$. $\mathbf{P}^{*\mathrm{T}}(0)$ is a transposed matrix of $\mathbf{P}(t)$ at initial time $t=0$.

Based on data from Tables II, VI, and VII, $\mathbf{P}^{*\mathrm{T}}(t)$ is solved as follows, and t represents time in 10^6 h

$$\boldsymbol{P}^{*\mathrm{T}}(t) = \begin{bmatrix} e^{-3.593t} \\ 0.17e^{-3.337t} - 0.17e^{-3.593t} \\ e^{-1.91t} - e^{-3.593t} \\ e^{-3.043t} - e^{-3.593t} \\ 0.3333e^{-3.467t} - 0.3333e^{-3.593t} \\ 0.3333e^{-3.467t} - 0.3333e^{-3.593t} \\ 0.1476e^{-3.593t} - 0.17e^{-3.337t} + 0.02244e^{-1.655t} \\ 0.06072e^{-3.593t} - 0.07284e^{-3.337t} + 0.01212e^{-2.055t} \\ 0.0187e^{-3.593t} - 0.05667e^{-3.337t} + 0.03797e^{-3.211t} \\ 0.0187e^{-3.593t} - 0.05667e^{-3.337t} + 0.03797e^{-3.211t} \\ 0.02244e^{-3.593t} - 0.17e^{-1.91t} + 0.1476e^{-1.655t} \\ 0.1853e^{-3.593t} - 0.4285e^{-1.91t} + 0.2432e^{-0.6283t} \\ 0.02322e^{-3.593t} - 0.3333e^{-1.91t} + 0.3101e^{-1.784t} \\ 0.02828e^{-3.593t} - 0.04399e^{-3.043t} + 0.01571e^{-2.055t} \\ 0.5675e^{-3.593t} - 0.6966e^{-3.043t} + 0.1291e^{-0.6283t} \\ 0.0008884e^{-3.593t} - 0.001553e^{-3.043t} + 0.000665e^{-2.31t} \\ 0.02983e^{-3.593t} - 0.04891e^{-3.043t} + 0.01908e^{-2.185t} \\ 0.02983e^{-3.593t} - 0.04891e^{-3.043t} + 0.01908e^{-2.185t} \\ 0.03797e^{-3.593t} - 0.05667e^{-3.467t} + 0.0187e^{-3.211t} \\ 0.13e^{-3.593t} - 0.1428e^{-3.467t} + 0.01278e^{-2.185t} \\ 0.03797e^{-3.593t} - 0.05667e^{-3.467t} + 0.0187e^{-3.211t} \\ 0.3101e^{-3.593t} + 0.02322e^{-1.784t} - 0.3333e^{-3.467t} \\ 0.13e^{-3.593t} - 0.1428e^{-3.467t} + 0.01278e^{-2.185t} \end{bmatrix}. \tag{8}$$

5) Reliability Metrics R(t) and MTTF: Then, calculating certain elements of matrix $\mathbf{P}(t)$ will finally get reliability function $R(t)$. Generally speaking, state transition diagram together with state probability matrix $\mathbf{P}(t)$ constitutes the system Markov reliability model.

Adding all elements of the $\mathbf{P}^{*\mathrm{T}}(t)$, reliability function $R_M(t)$ is obtained

$$\begin{aligned} R_M(t) = {} & 0.0682e^{-1.91t} - 0.05753e^{-3.593t} + 0.3333e^{-1.784t} \\ & - 0.06565e^{-3.467t} - 0.1862e^{-3.337t} \\ & + 0.17e^{-1.655t} + 0.1133e^{-3.211t} + 0.16e^{-3.043t} \end{aligned}$$

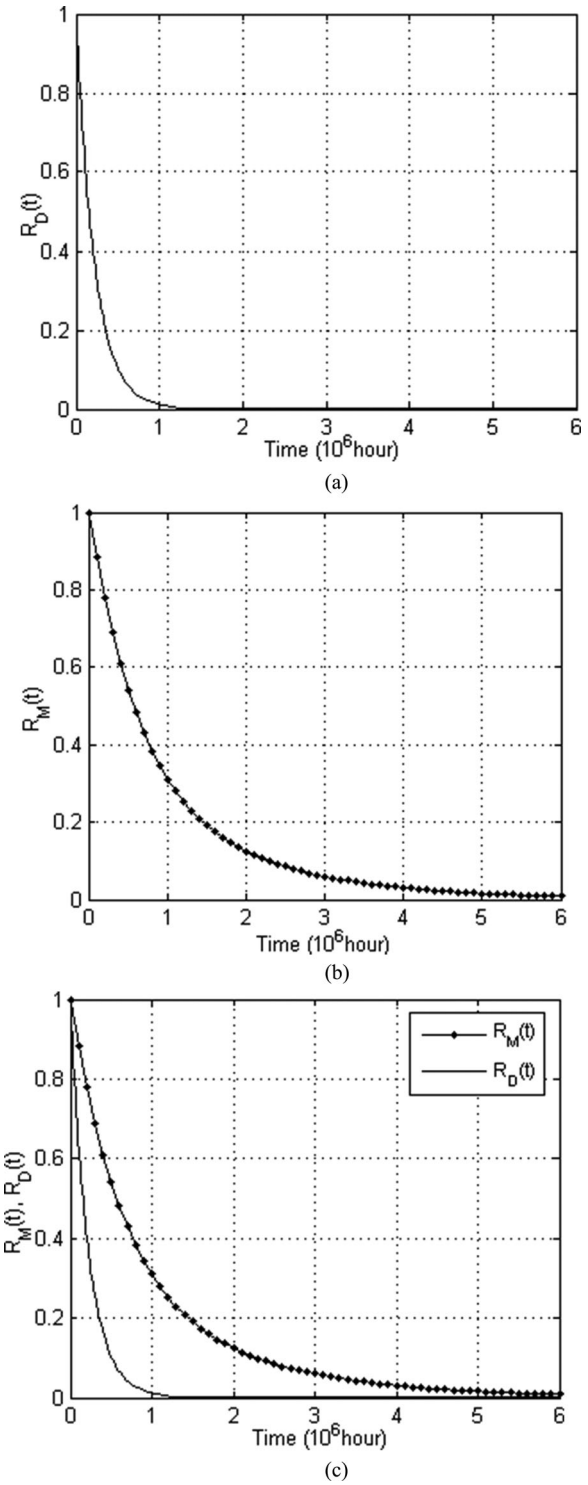

Fig. 4. Reliability function curves. (a) Function curve of $R_D(t)$. (b) Function curve of $R_{\rm M}(t)$. (c) Function curve comparison of $R_{\rm M}(t)$ and $R_D(t)$.

$$+ 0.3723e^{-0.6283t} + 0.000665e^{-2.31t} + 0.06373e^{-2.185t} + 0.02783e^{-2.055t} \quad (9)$$

where subscript *M* in $R_M(t)$ indicates that the reliability function is calculated by the Markov model, and *t* represents time in 10^6 h.

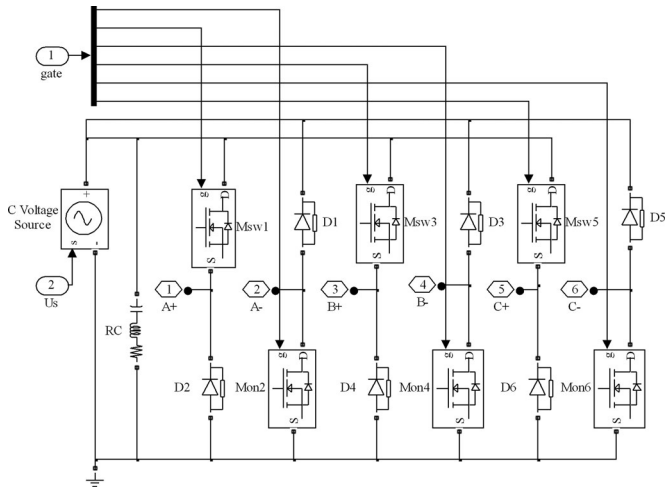

Fig. 5. Power converter simulation model.

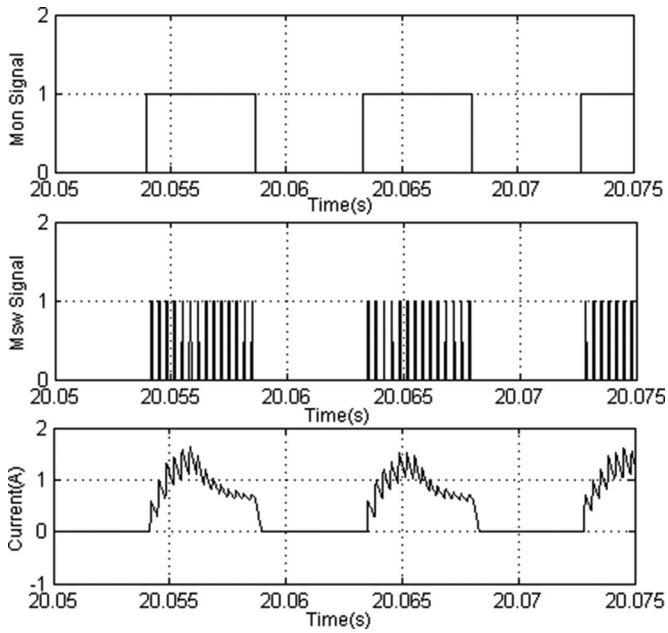

Fig. 6. Simulation results of *Phase A* MOSFET under normal condition: Mon2 drive signals (top), Msw*1* drive signals (middle) and current waveforms (1 A/div, bottom).

Referred to [14], [39], the MTTF is calculated as follows:

$$\mathrm{MTTF} = \int_0^\infty R_M(t)dt = 0.9579 \times 10^6 \mathrm{h} \quad (10)$$

as MTTF represents the average time of system operation without failures, then it can be concluded that the system is expected to operate for 0.9579×10^6 h, which provides time reference to fault detection and system maintenance.

C. Reliability Analysis of Binary Model and Multivariate One

Comparison of reliability indexes $R_M(t)$ and $R_D(t)$ is conducted, and function curves of $R_M(t)$ and $R_D(t)$ are shown in Fig. 4.

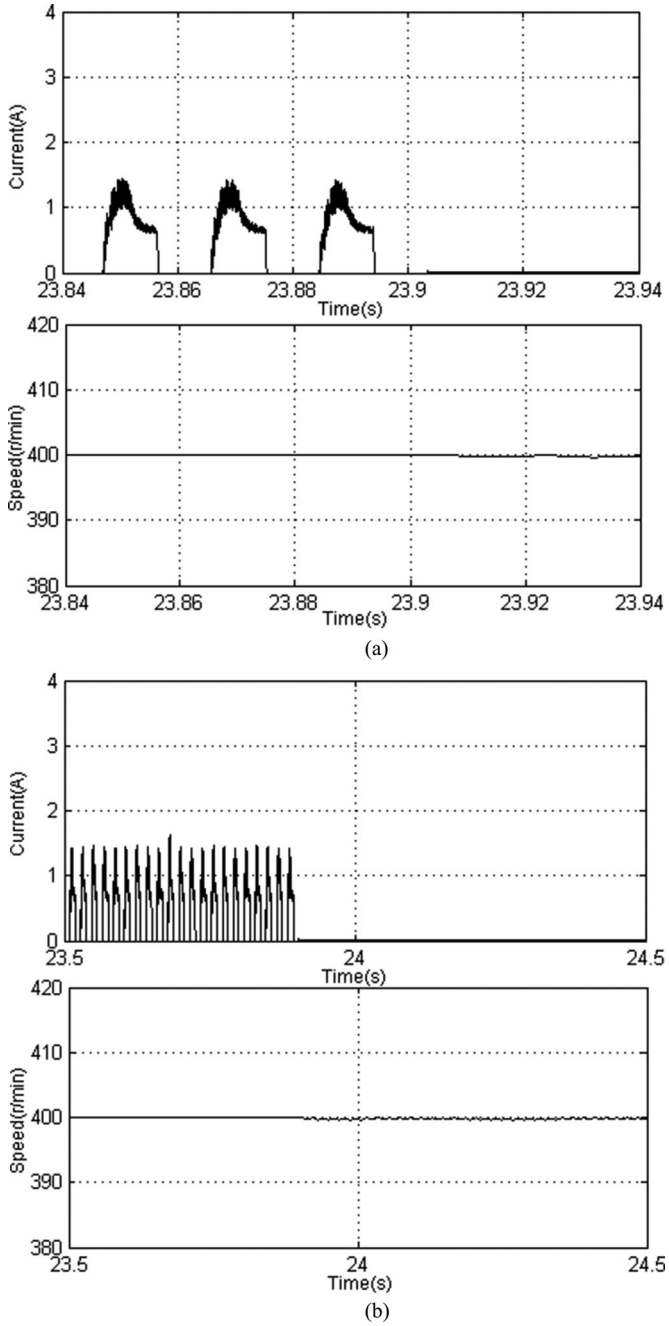

Fig. 7. Simulation results for MonO fault at $t = 23.9$ s: Current in fault phase (2 A/div), speed (20 r/min/div). (a) Waveforms of MonO fault at instantaneous moment. (b) Waveforms of MonO fault in a larger time interval.

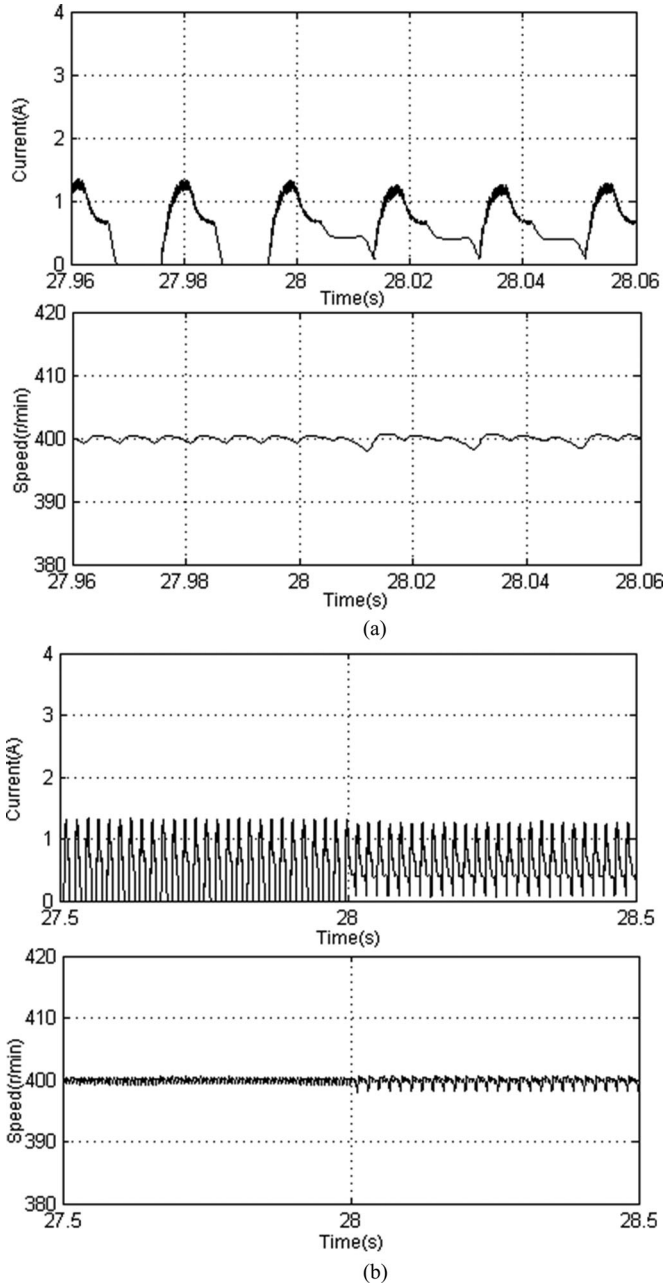

Fig. 8. Simulation results for MonS fault at $t = 28$ s: Current in fault phase (2 A/div), speed (20 r/min/div). (a) Waveforms of MonS fault at instantaneous moment. (b) Waveforms of MonS fault in a larger time interval.

It is shown in Fig. 4 that $R_{\mathrm{M}}(t)$ has a relatively high reliability compared with $R_D(t)$. It is inevitable that fault operation states are fully taken into account and, respectively, included in $R_{\mathrm{M}}(t)$ calculation. On the one hand, an RBD model believes that there are only operational states and failed ones in a system, so when a MonO fault occurs, the system will always be failed. However, the Markov model assesses system states based on the boundary and allows a second fault occurs in the survival system, which comes more in line with SRD operation condition. On the other hand, RBD considers that all the component faults are equivalent to cause the system to fail. In this case, the system will fail no matter a short circuit occurs in Mon or Msw, which cannot distinguish between the two components, and fail to reflect the effect of specific control strategy on system reliability. By contrast, the Markov model individually assesses the system state after each fault, the various system states can adequately reflect effects of each fault on the system reliability.

Hence, it is a successful attempt to conduct the reliability prediction of SRD based on the stochastic Markov process. The result also further demonstrates the superiority and accuracy

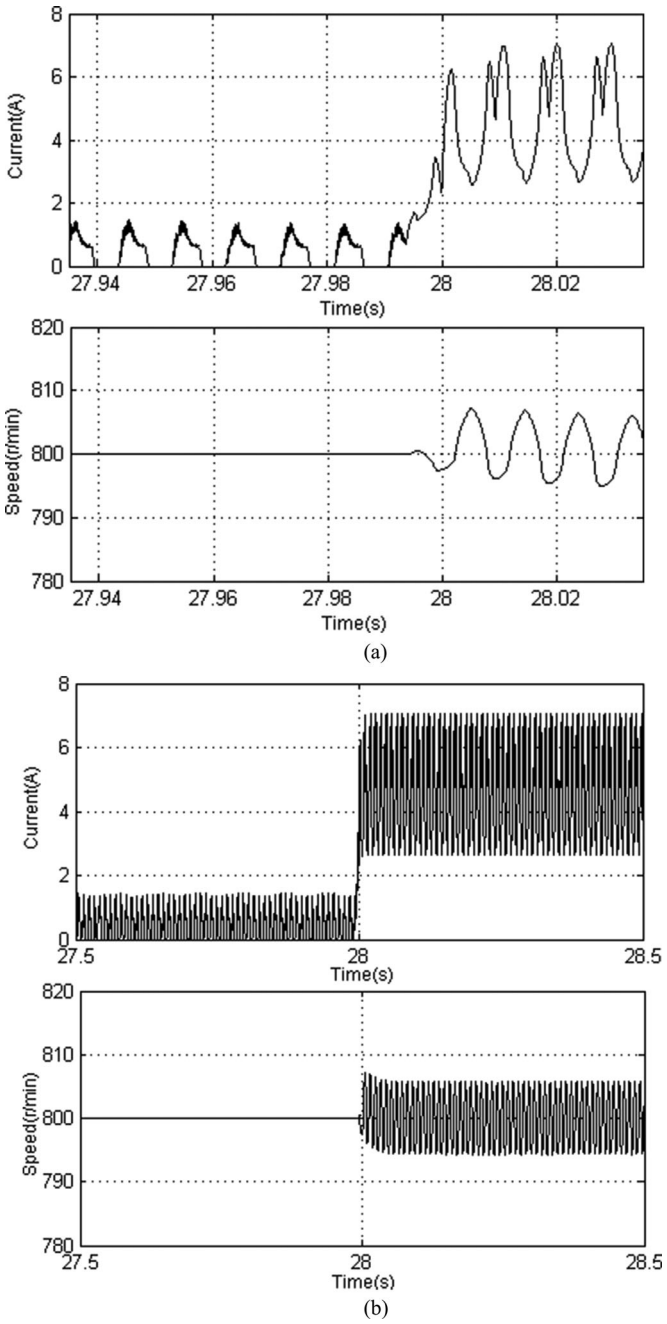

Fig. 9. Simulation results for MswS fault at $t = 27.9938$ s: Current in fault phase (2 /div), speed (20 r/min/div). (a) Waveforms of MswS fault at instantaneous moment. (b) Waveforms of MswS fault in a larger time interval.

of the dynamic-based Markov reliability model applied in a repairable system.

IV. Simulation Analysis and Experimental Verification

A. Simulation Analysis of SRD

Three-phase 12/8 switched reluctance motor and asymmetrical half-bridge power converter are selected, and system simulation parameters are consistent with the rated parameters of SRD prototype in Section III. Simulation model is built in MATLAB/Simulink environment and components are selected

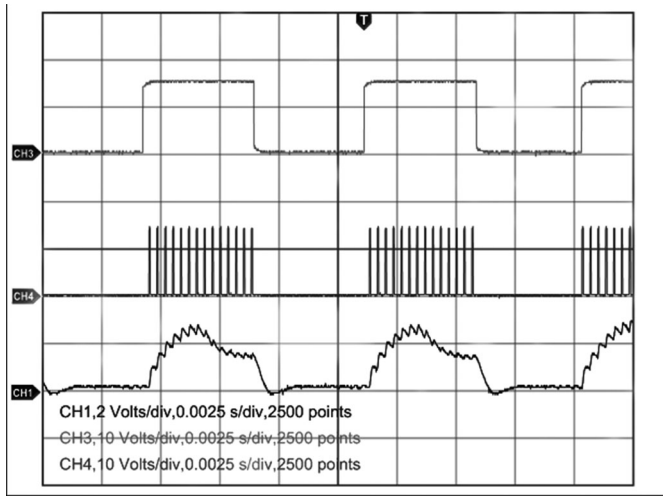

Fig. 10. Experimental results of *Phase A* MOSFET under normal condition: Mon2 drive voltages signals (CH3, 10 V/div, top), Msw*1* drive voltages signals (CH4, 10 V/div, middle) and current waveforms (CH1, 1A/div, bottom).

directly from the Simulink blocks. The power converter simulation model is shown in Fig. 5. Here, *C voltage source* is controllable voltage source controlled by a given voltage *Us* and providing voltage to the dc bus capacitor *RC*. The terminals *A*, *B,* and *C* represent windings of three phases, and they possess basically the same circuit structure. Take phase *A* as an example, *A*+ and *A*– are the connection ports at both ends of phase *A* windings; Msw*1* and Mon*2* are, respectively, for the upper and lower MOSFET; *D1* and *D2* are freewheeling diodes. The *gate* port provides signal for MOSFETs.

Running the system simulation model under normal condition without faults, then gate drive voltage waveforms together with phase current waveforms can be achieved. Fig. 6 shows drive signals for Msw1 and Mon2, and *Phase A* current waveforms at speed of 800 r/min. In Fig. 6, when the photoelectric switch connected with *Phase A* is ON, the *Mon Signal* keeps at high level and triggers the transistor Mon*2* to switch on. At the same time, Msw *Signal* is modulated by PWM and commands Msw*1* to start chopping. Consequently, *Phase A* current produces and begins to rising. With the rotation of rotor, *Phase A* photoelectric switch turns OFF, then drive signals for Msw1 and Mon*2* become low level. Afterward, *Phase A* turns into off-state and current in *Phase A* falls into 0 until the next cycle drive signal comes.

The fault modes in Table I are individually injected into the system, followed by the detection of speed and current, which are compared with performance metrics in Table III, then the system state is determined. When the system survives, another different component fault mode is injected to continue the state assessment until the system fails completely. Here, the fault modes PD, MonS, and MswS are simulated to show how the state assessment conducted.

Assuming a PD fault has occurred, taking MonO as an example, waveforms of speed and current in faulted phase are shown in Fig. 7(a) and (b). Simulation runs at speed of 400 r/min and fault is injected at $t = 23.9$ s under system steady-state operation. It is shown in Fig. 7(a) that the current fluctuation is within the boundary. In Fig. 7(b), the system keeps running with slight

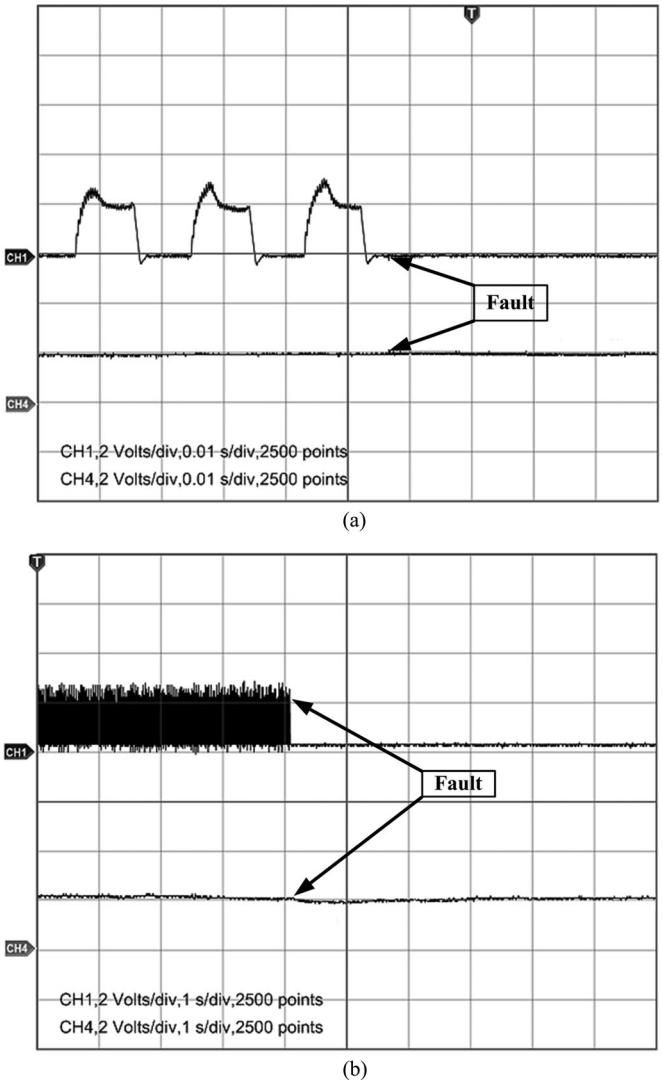

Fig. 11. Experimental results for MonO fault at 400 r/min: current in fault phase (CH1, 1 A/div, top) and speed (CH4, 400 r/min/div, bottom). (a) Waveforms of MonO fault at instantaneous moment. (b) Waveforms of MonO fault in a larger time interval.

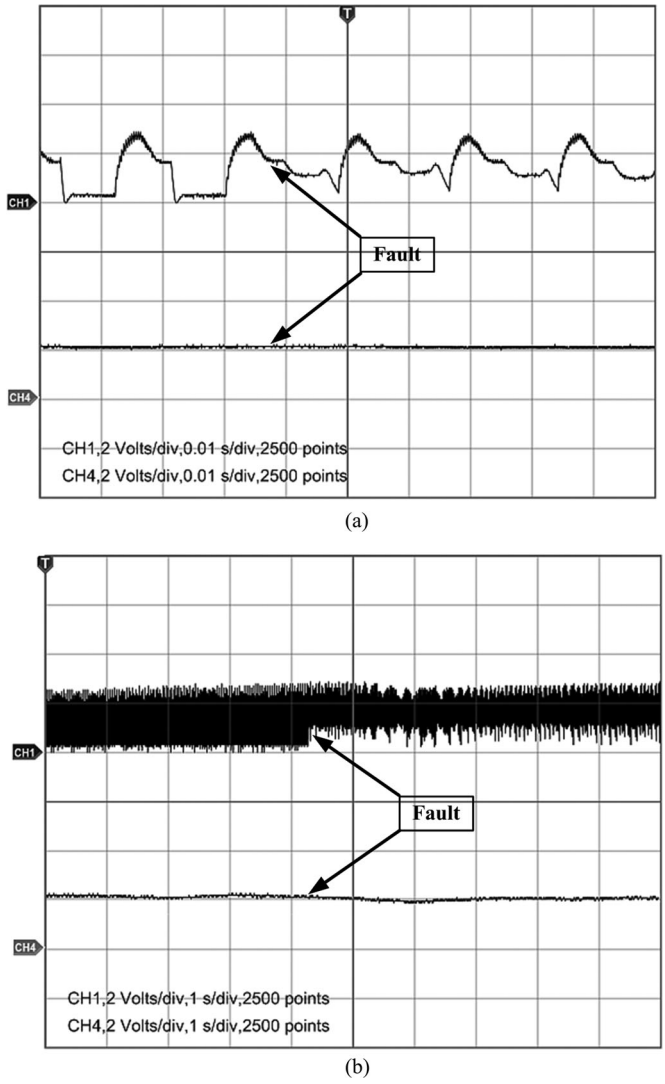

Fig. 12. Experimental results for MonS fault at 400 r/min: current in fault phase (CH1, 1 A/div, top) and speed (CH4, 400 r/min/div, bottom). (a) Waveforms of MonS fault at instantaneous moment. (b) Waveforms of MonS fault in a larger time interval.

speed fluctuation, and the speed fluctuation does not exceed the acceptable range owing to the control strategy. As a result, the system is able to continue running and system state is judged to be "survival state." Fig. 8(a) and (b) shows that an MonS fault is occurred at $t = 28$ s and system runs at 400 r/min. It is obvious that the fluctuation of speed and current both are within the boundary, thus obtaining a "survival state" too. Fig. 9(a) and (b) displays an example of a system "failed state" with an MswS fault occurred at $t = 27.9938$ s at 800 r/min. Fig. 9(a) shows current and speed waveforms at instantaneous moment of fault occurrence, while Fig. 9(b) gives waveforms in a larger time interval, which considers that failed state severely damages system normal operation and it takes longer time for system to recovery steady operation. Once the MswS fault occurs, current fluctuation exceeds the allowable boundary, which results in a "failed state."

B. Experimental Validation

A three-phase switched reluctance motor with 12/8 structure is selected to implement the experiment. It is worth mentioning that the current sensor gets voltage signal initially, and then transits it into current, so the current waveforms gotten from the oscilloscope are expressed with units of voltage, shown as *volts* in the following figures from Figs. 10 to 13. Here, the conversion ratio between the voltage and current is 2:1. Also, speed is achieved from voltage detection, and 1 voltage would be transited into 200 r/min. Fig. 10 displays the experimental results of *Phase A* current and transistors drive voltages under normal condition at 800 r/min. In contrast to the simulation results of Fig. 6, waveform trends of the two are basically consistent and the goodness of fit is well, which indicates the availability of simulation models. Then a "survival state" MonO fault is conducted, results are shown in Fig. 11. There is a slight overshoot of system speed, but compared with Fig. 7, it can be seen that

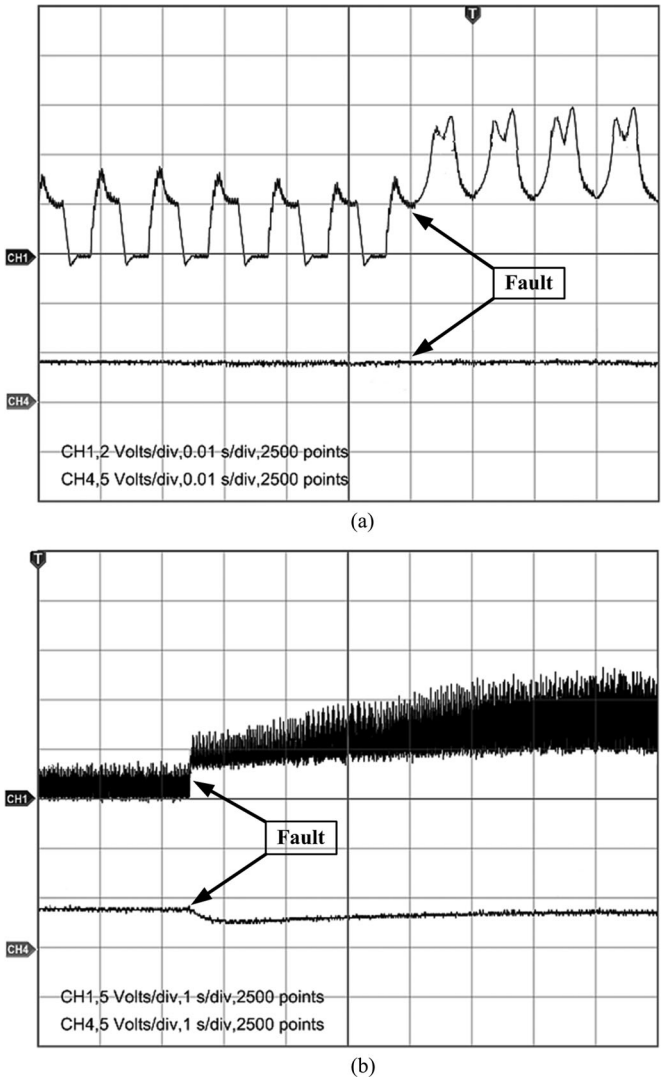

Fig. 13. Experimental results for MswS fault at 800 r/min. (a) Waveforms of MswS fault at instantaneous moment: Current in fault phase (CH1, 1 A/div, top) and speed (CH4, 1000 r/min/div, bottom).(b) Waveforms of MswS fault in a larger time interval: Current in fault phase (CH1, 2.5 A/div, top) and speed (CH4, 1000 r/min/div, bottom).

simulation and experiment results fits well. Fig. 12 provides another system "survival state" under MonS fault, whose operation conditions are corresponding to those in Fig. 8. Fig. 13 illustrates a system "failed state" under MswS fault, which basically displays consistency with Fig. 9. Fig. 13(a) shows instantaneous change in fault phase current, while Fig. 13(b) illustrates waveforms in a larger time interval. Compared with Fig. 9(b), the waveforms rise more slowly under the influence of mechanical friction and rotational inertia. Besides, due to restrictions on the oscilloscope display range, the values of *Volts/div* in CH1 and CH4 are adjusted accordingly to show a complete waveform. It is clear that both current and speed fluctuation exceed the boundary. Hence, system falls into a "failed state."

From the above experimental results, it can be shown that short circuit occurred in Msw (MswS) and Mon (MonS) has different effects on the system performance due to the different functions. Since single switch chopping strategy is adopted, MswS fault makes the switch Msw unable to implement chopping. In this case, a larger current remained in the fault phase will periodically generate braking torque, thus seriously affecting the system performance. In contrast, after MonS fault the phase can still perform normally during the on period of fault phase, and abnormal operation appears only in freewheeling commutation interval. Due to the specific control strategy, system performance under MswS and MonS fault differs from each other. Simulation and experimental results confirm the impacts of specific control strategy. Also, results verify the accuracy of system state evaluation.

V. Conclusion

This paper presents a specific set of reliability prediction methodology for SRD, which covers the impact of specific control strategy as well as component fault classification. The methodology is conducted from component-level fault analysis to system-level reliability modeling. At component level, components in SRD system are divided into different types according to their functions not their own categories. Also, the specific component-level fault classification and summary are conducted to identify dominant fault modes in SRD. Five kinds of fault modes are collected as one PD fault, which is a new element in the subsequent reliability modeling. At system level, an RBD reliability and the Markov reliability model are adopted and compared to illustrate the reliability prediction process. Specifically, the system state transition diagram is presented to show a graphical Markov model, and state probability matrix is achieved by detailed calculation to represent a numerical Markov model. Results show that the Markov model can capture the effect of specific control strategy on system reliability and solve the inequivalence problem of component fault and system failure.

Further research can focus on the variation of failure rate under different kinds of system fault modes compensating the insufficient that constant failure rate ignores the temperature rise in faulted component. Since the impact on system operation state caused by control strategy is illustrated, more extended work can be carried out to quantify this influence. Also, the performance metrics can be extended, which will help to improve the applicability of the model. Since this paper accomplishes the task of evaluating the SRD reliability in numerical and graphic method, it contributes to providing a more intuitive reliability model that captures effects of a control strategy for repairable the system. Also, fault classification based on component function is worth popularizing.

References

[1] J. Cai and Z. Deng, "Sensorless control of switched reluctance motor based on phase inductance vectors," *IEEE Trans. Power Electron.*, vol. 27, no. 7, pp. 3410–3423, Jul. 2012.

[2] J. F. Pan, Y. Zou, N. Cheung, and G. Cao, "On the voltage ripple reduction control of the linear switched reluctance generator for wave energy utilization," *IEEE Trans. Power Electron.*, vol. 29, no. 10, pp. 5298–5307, Oct. 2014.

[3] M. D. Hennen, M. Niessen, C. Heyers, H. J. Brauer, and R. W. De Doncker, "Development and control of an integrated and distributed inverter for a fault tolerant five-phase switched reluctance traction drive," *IEEE Trans. Power Electron.*, vol. 27, no. 2, pp. 547–554, Feb. 2012.

[4] M. Krishnamurthy, C. Edrington, A. Emadi, P. Asadi, M. Ehsani, and B. Fahimi, "Making the case for applications of switched reluctance motor technology in automotive products," *IEEE Trans. Power Electron.*, vol. 21, no. 3, pp. 659–675, May 2006.
[5] L. Szabó and M. Ruba, "Segmental stator switched reluctance machine for safety-critical applications," *IEEE Trans. Ind. Appl.*, vol. 48, no. 6, pp. 2223–1229, Nov./Dec. 2012.
[6] D. Hirschmann, D. Tissen, S. Schroder, and R. W. DeDoncker, "Reliability prediction for inverters in hybrid electrical vehicles," *IEEE Trans. Power Electron.*, vol. 22, no. 6, pp. 2511–2517, Nov. 2007.
[7] A. K. Verma, S. Ajit, and D. R. Karanki, *Reliability and Safety Engineering*, 1st ed. New York, NY, USA: Springer, 2010.
[8] Y. Song and B. Wang, "Survey on reliability of power electronic systems," *IEEE Trans. Power Electron.*, vol. 28, no. 1, pp. 591–604, Jan. 2013.
[9] B. Foucher, J. Boullie, B. Meslet, and D. Das, "A review of reliability prediction methods for electronic devices," *Microelectron. Reliab.*, vol. 42, no. 8, pp. 1155–1162, Aug. 2002.
[10] A. Goel and R. J. Graves, "Electronic system reliability: collating prediction models," *IEEE Trans. Device Mater. Rel.*, vol. 6, no. 2, pp. 258–265, Jun. 2006.
[11] A. Testa, S. De Caro, and S. Russo, "A reliability model for power MOSFETs working in avalanche mode based on an experimental temperature distribution analysis," *IEEE Trans. Power Electron.*, vol. 27, no. 6, pp. 3093–3100, Jun. 2012.
[12] W. Zhang, D. Xu, P. N. Enjeti, H. Li, J. T. Hawke, and H. S. Krishnamoorthy, "Survey on fault-tolerant techniques for power electronic converters," *IEEE Trans. Power Electron.*, vol. 29, no. 12, pp. 6319–6331, Dec. 2014.
[13] M. J. Cushing, D. E. Mortin, T. J. Stadterman, and A. Malhotra, "Comparison of electronics reliability assessment approaches," *IEEE Trans. Rel.*, vol. 42, no. 4, pp. 542–546, Dec. 1993.
[14] M. Rausand and A. Høyland, *System Reliability Theory: Models, Statistical Methods, and Applications*, 2nd ed. Hoboken, NJ, USA: Wiley, 2005.
[15] S. E. D. Leon-Aldaco, H. Calleja, F. Chan, and H. R. Jimenez-Grajales, "Effect of the mission profile on the reliability of a power converter aimed at photovoltaic applications—A case study," *IEEE Trans. Power Electron.*, vol. 28, no. 6, pp. 2998–3007, Jun. 2013.
[16] M. Anthony, R. Arno, and N. Dowling, "Reliability analysis for power to fire pump using fault tree and RBD," *IEEE Trans. Ind. Appl.*, vol. 49, no. 2, pp. 997–1003, Mar./Apr. 2013.
[17] F. Richardeau and T. T. L. Pham, "Reliability calculation of multilevel converters: Theory and applications," *IEEE Trans. Ind. Electron.*, vol. 60, no. 10, pp. 4225–4233, Oct. 2013.
[18] E. Koutroulis and F. Blaabjerg, "Design optimization of transformerless grid-connected PV inverters including reliability," *IEEE Trans. Power Electron.*, vol. 28, no. 1, pp. 325–335, Jan. 2013.
[19] H. Shaker, H. Zareipour, and M. Fotuhi-Firuzabad, "Reliability modeling of dynamic thermal rating," *IEEE Trans. Power Electron.*, vol. 28, no. 3, pp. 1600–1609, Jan. 2013.
[20] S. V. Dhople and A. D. Dominguez-Garcia, "Estimation of photovoltaic system reliability and performance metrics," *IEEE Trans. Power Syst.*, vol. 27, no. 1, pp. 554–563, Feb. 2012.
[21] M. Molaei, H. Oraee, and M. Fotuhi-Firuzabad, "Markov model of drive motor systems for reliability calculation," in *Proc. IEEE Int. Symp. Ind. Electron.*, Jul. 2006, pp. 2286–2291.
[22] A. M. Bazzi, A. D. Dominguez-Garcia, and P. T. Krein, "A method for impact assessment of faults on the performance of field-oriented control drives: a first step to reliability modeling," in *Proc. IEEE Appl. Power Electron. Conf. Expo.*, 2010, pp. 256–263.
[23] A. M. Bazzi, A. D. Dominguez-Garcia, and P. T. Krein, "Markov reliability modeling for induction motor drives under field-oriented control," *IEEE Trans. Power Electron.*, vol. 27, no. 2, pp. 534–546, Feb. 2012.
[24] K. Jiang and C. Singh, "New models and concepts for power system reliability evaluation including protection system failures," *IEEE Trans Power Syst*., vol. 26, no. 4, pp. 1845–1855, Nov. 2011.
[25] S. V. Dhople and A. D. Domínguez-García, "Estimation of photovoltaic system reliability and performance metrics," *IEEE Trans Power Syst*., vol. 27, no. 1, pp. 1845–1855, Nov. 2011.
[26] S. Gopalakrishnan, A. M. Omekanda, and B. Lequesne, "Classification and remediation of electrical faults in the switched reluctance drive," *IEEE Trans. Ind. Appl.*, vol. 42, no. 2, pp. 479–486, Mar./Apr. 2006.
[27] H. Wang, S. Pekarek, and B. Fahimi, "Multilayer control of an induction motor drive: A strategic step for automotive applications," *IEEE Trans. Power Electron.*, vol. 21, no. 3, pp. 676–686, May 2006.
[28] H. Berriri, M. W. Naouar, and I. Slama-Belkhodja, "Easy and fast sensor fault detection and isolation algorithm for electrical drives," *IEEE Trans. Power Electron.*, vol. 27, no. 2, pp. 490–499, Feb. 2012.
[29] A. B. Youssef, S. K. El Khil, and I. Slama-Belkhodja, "State observer-based sensor fault detection and isolation, and fault tolerant control of a single-phase PWM rectifier for electric railway traction," *IEEE Trans. Power Electron.*, vol. 28, no. 12, pp. 5842–5853, Dec. 2013.
[30] H. Chen and S. Lu, "Fault diagnosis digital method for power transistors in power converters of switched reluctance motors," *IEEE Trans. Ind. Electron.*, vol. 60, no. 2, pp. 749–763, Feb. 2013.
[31] N. S. Gameiro and A. J. M. Cardoso, "A new method for power converter fault diagnosis in SRM drives," *IEEE Trans. Ind. Appl.*, vol. 48, no. 2, pp. 653–662, Mar./Apr. 2012.
[32] Q. T. An, L. Z. Sun, K. Zhao, and L. Sun, "Switching function model-based fast-diagnostic method of open-switch faults in inverters without sensors," *IEEE Trans. Power Electron.*, vol. 26, no. 1, pp. 119–126, Jan. 2011.
[33] F. Aghili, "Fault-tolerant torque control of BLDC motors," *IEEE Trans. Power Electron.*, vol. 26, no. 2, pp. 355–363, Feb. 2011.
[34] A. Tani, M. Mengoni, L. Zarri, G. Serra, and D. Casadei, "Control of multiphase induction motors with an odd number of phases under open-circuit phase faults," *IEEE Trans. Power Electron.*, vol. 27, no. 2, pp. 565–577, Feb. 2012.
[35] A. Sayed-Ahmed and N. A. O. Demerdash, "Fault-tolerant operation of delta-connected scalar- and vector-controlled AC motor drives," *IEEE Trans. Power Electron.*, vol. 27, no. 6, pp. 3041–3049, Jun. 2012.
[36] S. M. Jung, J. S. Park, H. W. Kim, K. Y. Cho, and M. J. Youn, "An MRAS-based diagnosis of open-circuit fault in PWM voltage-source inverters for PM synchronous motor drive systems," *IEEE Trans. Power Electron.*, vol. 28, no. 5, pp. 2514–2526, May 2013.
[37] U. M. Choi, H. G. Jeong, K. B. Lee, and F. Blaabjerg, "Method for detecting an open-switch fault in a grid-connected NPC inverter system," *IEEE Trans. Power Electron.*, vol. 27, no. 6, pp. 2726–2739, Jun. 2012.
[38] H. Y. Long, N. L. King, M. R. Sweet, and E. M. S. Narayanan, "Numerical evaluation of the short-circuit performance of 3.3-kV CIGBT in field-stop technology," *IEEE Trans. Power Electron.*, vol. 27, no. 5, pp. 2673–2679, May 2012.
[39] *Military Handbook Reliability Prediction of Electronics Equipment*, US Department of Defense, MIL-HDBK-217 F, 1995.
[40] *Reliability Prediction Handbook for Electronic Equipment*, Chinese PLA General Armament Department, GJB/Z 299C, 2006.
[41] S. V. Dhople, A. Davoudi, A. D. Dominguez-Garcia, and P. L. Chapman, "A unified approach to reliability assessment of multiphase DC–DC converters in photovoltaic energy conversion systems," *IEEE Trans. Power Electron.*, vol. 27, no. 2, pp. 739–751, Feb. 2013.
[42] S. Harb and R. S. Balog, "Reliability of candidate photovoltaic module-integrated-inverter (PV-MII) topologies-a usage model approach," *IEEE Trans. Power Electron.*, vol. 28, no. 6, pp. 3019–3027, Jun. 2013.

Hao Chen (SM'08) received the B.S. and Ph.D. degrees from the Department of Automatic Control, Nanjing University of Aeronautics and Astronautics, Nanjing, China, in 1991 and 1996, respectively.

In 1998, he became an Associate Professor with the School of Information and Electrical Engineering, China University of Mining and Technology, Xuzhou, China. From 2002 to 2003, he was a Visiting Professor with Kyungsung University, Busan, Korea. Since 2001, he has been a Professor with the School of Information and Electrical Engineering, China University of Mining and Technology. Since 2008, he has also been an Adjunct Professor with the University of Western Australia, Perth, W.A., Australia. He is the author of one book and has also authored more than 170 papers. He is the holder of 18 Chinese invention patents, six Chinese utility model patents, and one Danish invention patent. His current research interests include motor control, linear launcher, electric vehicles, electric traction, servo drives, and wind power generator control.

Prof. Chen received the Prize of Science and the Technology of Chinese Youth and the Prize of the Fok Ying Tong Education Foundation for Youth Teachers both in 2004. He received the second prize in the Science and Technology advanced of Province and Ministry six times, and the third prize in the Science and Technology Advanced of Province and Ministry 12 times. He became the Chinese New Century Hundred-Thousand-Ten thousand Talents Engineering National Talent in 2007, and received the Government Especial Allowance of People's Republic of China State Department since 2006.

Huan Yang received the B.S. degree in electrical engineering from the China University of Mining and Technology, Xuzhou, China, in 2012. She is currently working toward the Master's degree in electrical engineering from the China University of Mining and Technology, Xuzhou, China.

Her research interest includes motor reliability.

Yuxiang Chen received the B.S. and M.S. degrees in power electronic and power transmission from the China University of Mining and Technology, Xuzhou, China, in 2011 and 2014, respectively. She is currently working toward the Ph.D. degree in power electronic and power transmission from Zhejiang University, Hangzhou, China. Her research interest includes component testing.

Herbert Ho-Ching Iu (S'98–M'00–SM'06) received the B.Eng.(Hons.) degree in electrical and electronic engineering from the University of Hong Kong, Pokfulam, Hong Kong, China, in 1997, and the Ph.D. degree from the Hong Kong Polytechnic University, Hung Hom, Hong Kong, in 2000.

In 2002, he joined the School of Electrical, Electronic and Computer Engineering, The University of Western Australia, Crawley, W.A., Australia, as a Lecturer, where he is currently a Professor. He has published more than 100 papers in these areas. He is a Coeditor of *Control of Chaos in Nonlinear Circuits and Systems* (Singapore: World Scientific, 2009) and a coauthor of *Development of Memristor Based Circuits* (Singapore: World Scientific, 2013). His research interests include power electronics, renewable energy, nonlinear dynamics, current sensing techniques, and memristive systems.

Prof. Iu received the two IET Premium Awards in 2012 and 2014. In 2014, he also received the Vice-Chancellor's Mid-Career Research Award. He currently serves as an Associate Editor for the *International Journal of Bifurcation and Chaos*, the *IEEE Circuits and Systems Society Newsletters*, the *IET Power Electronics* and *International Journal of Electronics*, and an Editorial Board Member for the *International Journal of Circuit Theory and Applications*.